Surface Evolution of Lithium Titanate upon Electrochemical Cycling using a Combination of Surface Specific Characterization Techniques

Jokin Rikarte, Begoña Acebedo, Arantxa Vilalta-Clemente, Francisco Bonilla, Angus J. Wilkinson, Montserrat Galceran, Arturo Lousa, Juan Rubio-Zuazo, Miguel Ángel Muñoz-Márquez

Authors Accepted Manuscript of Article to be published in

Advanced Materials Interfaces
2020

Surface Evolution of Lithium Titanate upon Electrochemical Cycling using a Combination of Surface Specific Characterization Techniques

*Jokin Rikarte, Begoña Acebedo, Arantxa Vilalta-Clemente, Francisco Bonilla, Angus J. Wilkinson, Montserrat Galceran, Arturo Lousa, Juan Rubio-Zuazo, Miguel Ángel Muñoz-Márquez**

J. Rikarte, B. Acebedo, Dr. F. Bonilla, Dr. M. Galceran, Dr. M. A. Muñoz-Márquez
CIC energiGUNE
Albert Einstein 48, 01510 Miñano, Spain.
E-mail: mamunoz@cicenergigune.com

J. Rikarte[+]
Departamento de Física de la Materia Condensada
Facultad de Ciencia y Tecnología
Universidad del País Vasco, UPV/EHU
P.O. Box 644, 48080 Bilbao, Spain
[+] Current address: OXIS Energy Ltd, E1 Culham Science Centre, OX14 3DB Abingdon, Oxfordshire, United Kingdom

Dr. A. Vilalta-Clemente[++], Prof. A. J. Wilkinson
Department of Materials
University of Oxford
16 Parks Road, Oxford OX1 3PH, UK
[++] Current address: Institut Pprime, CNRS, ENSMA, Université de Poitiers, UPR CNRS 3346, Physics and Mechanics of Material Department, ENSMA, Téléport 2, 1 avenue Clément Ader, BP 40109, 86961 Futuroscope Chasseneuil Cedex, France

Dr. A. Lousa
Department de Física Aplicada
Universitat de Barcelona
Martí i Franquès 1, 08028 Barcelona, Spain

Dr. J. Rubio-Zuazo
SpLine, Spanish CRG BM25 Beamline
The European Synchrotron (ESRF)
71 Avenue des Martyrs, 38000 Grenoble, France

Dr. J. Rubio-Zuazo
Instituto de Ciencia de Materiales de Madrid
Consejo Superior de Investigaciones Científicas (ICMM-CSIC)
Sor Juana Inés de la Cruz, 3, 28049, Madrid, Spain

Keywords: $Li_4Ti_5O_7$, surface reactivity, HREBSD, XPS, HRTEM

Abstract.

Among the commercial materials used as electrodes for Li-ion batteries, $Li_4Ti_5O_{12}$ (LTO) stands out as anode for stationary applications owing to its stability and safety, in part ascribed to its low surface reactivity that prevents the formation surface layers always present in other negative electrode materials. However, the existence of activity on the LTO surface upon electrochemical cycling has been reported in recent years; the formation of a rough surface layer of electrochemically inactive α-Li_2TiO_3 on top of the LTO (111) surface is suggested on the grounds of scanning probe techniques and theoretical ab-initio calculations which, if confirmed, negatively strikes on the battery performance. Hence the investigation of the LTO surface evolution is key to achieve more stable and safer Li-ion batteries. LTO (111) thin film electrodes are used as model system where a wide variety of surface specific, local and long-range, characterization techniques are applied to unveil the surface behavior of LTO in Li-ion batteries. In contrast with previous studies, with the help of high resolution transmission electron microscopy and synchrotron-based surface X-ray diffraction, α-Li_2TiO_3 is found to be a surface preparation product, hence not formed upon cycling. Of special importance is the use of high resolution electron backscatter diffraction to report an increase on the LTO surface strain upon electrochemical cycling which can have a critical effect in long cycling performance of LTO always considered a zero-strain material.

1. Introduction

Rechargeable Lithium-ion batteries are widely known to be the dominant energy storage system for electronic devices and power tools,[1,2] they are currently the best option for Electric Vehicles (EV)[3,4] and they are also used for grid storage.[5,6] Since their commercialization in the 1990s, the most conventional Li-ion battery has been composed by graphite as anode and $LiCoO_2$ as cathode materials.[2] However, during the last years, other electrode materials have been studied and commercialized.[7,8] Among them, $Li_4Ti_5O_{12}$

(LTO)[9,10] is one of the potential alternatives to the graphite as anode material, which despite delivering only 45% of the specific capacity of graphite has reached the commercial stage owing to its outstanding performance in terms of high current rate, stability and safety.

LTO has a defective spinel structure ($Fd\bar{3}m$ space group) with the oxygen atoms forming a face-centered cubic (fcc) lattice. Upon lithiation, three lithium ions per formula unit are intercalated to form the rock salt analogue structured phase $Li_7Ti_5O_{12}$,[11,12] leading into a theoretical specific capacity of 175 mA h g^{-1}. Three main features can be highlighted for this negative electrode material: first, the small volume change between the spinel and the rock salt structures, less than 0.1%,[12–16] which minimize the electrode degradation caused by mechanical strain and enables the long and stable cycle life reported for LTO electrodes.[17–19] Second, the much lower release of heat of the LTO electrode during lithiation if compared with graphite-based electrodes. Third, the insertion potential at 1.55 V vs Li^+/Li which prevents the Li plating and should prevent the organic electrolyte reduction, that typically occurs below 1.0 V vs Li^+/Li.[20–22] All these features have made of LTO an interesting anode material for rechargeable Li-ion batteries in general, and for high power applications and long cycle life applications[17,23–27] in particular, e.g. hybrid EV, plug-in hybrid EV and peak shaving in the electric grid. Unfortunately, despite the outstanding performance of LTO electrodes, the gassing reported during charge/discharge cycles and storage, especially at elevated temperatures, can hinder the interest of power Li-ion battery industry on LTO-based batteries.

From the first work on LTO spinel anodes reported by Thackeray and co-workers almost 25 years ago, many studies can be found in the bibliography related to LTO synthesis paths,[28–38] as well as coating[39–42] and doping[43–45] processes for improving the cycling performance of the LTO material. However, not much interest was initially shown regarding the investigation of the LTO surface as it was thought to be a solid electrolyte interphase (SEI)-free electrode

owing to its high insertion potential. Only in the last decade, different studies confirmed that LTO is not free from surface reactions.[46–55]

It has been in the last five years when, besides the formation of new compounds in the electrode-electrolyte interphase via decomposition reactions, the evolution of the LTO surface itself has attracted much of the attention. Several investigations have resulted in different interpretations of the LTO surface and interface evolution. Y.-B. He and co-workers have reported, by means of transmission electron microscopy (TEM), the transformation of the outermost LTO (111) planes into (222) planes and formation of anatase TiO_2 (101), the latter ones being a result of the spontaneous reactions between LTO and the electrolyte.[49] Meanwhile, also based on TEM experiments and ab-initio calculations, X. Lu et al. have concluded that Li ions occupy different sites on lithiation/delithiation and a sharp interface separates the $Li_4Ti_5O_{12}$ and $Li_7Ti_5O_{12}$ domains; in this study there is no evidence of formation of anatase TiO_2.[56] The insertion of an excess of lithium in the near surface region has been reported by F. Wang et al as a result of TEM and electron energy loss spectroscopy (EELS) experiments.[57] M. Kitta and co-workers described the possible formation of α-Li_2TiO_3 phase on the surface of LTO upon first Li ion insertion-extraction along with an increase of the surface corrugation, on the grounds of a TEM, EELS and atomic force microscopy (AFM) investigation, suggesting that it could work as a protective layer.[58] Recent ab-initio calculations suggest that the formation of this lithium metatitanate phase on top of the lithium titanate could occur under certain conditions; starting from $Li_4Ti_5O_{12}$, the α-Li_2TiO_3 phase could be formed either a) during the 1st Li-insertion, or b) during the 1st Li-extraction, following reaction with Li_2O formed during the 1st Li-insertion.[59]

Given the importance of the understanding of the LTO surface and interface evolution and considering that the vast majority of surface studies have been performed using experimental techniques which deliver information on the local structure and composition, we have synthesized highly oriented LTO (111) thin films, free of conductive additives and binders,

which have been electrochemically cycled. This model system will allow the controlled study of the LTO surface evolution upon lithiation/delithiation by means of local techniques such as cross-section TEM and long range surface specific characterization techniques such as X-ray photoelectron spectroscopy (XPS), surface X-ray diffraction (XRD) in a synchrotron source and high resolution electron backscatter diffraction (HREBSD) an experimental technique used in the study of metals, semiconductors and geological material which, here to our knowledge, has been used for the first time in the study of battery materials. The HREBSD is the cross correlation based in EBSD[60] analysis approach introduced by Wilkinson improving the angular resolution from ~1º to 0.005º by measuring small shifts of features in the EBSD pattern compared to a reference EBSD pattern. These small shifts can be interpreted in terms of lattice rotation and lattice distortions.[61–64] As a result of this multimodal charaterisation, we have proven that the α-Li_2TiO_3 phase is present in the pristine LTO and is not a result of the electrochemical process as previously reported.[58] Moreover, we have determined a significant increase in the surface strain of LTO upon cycling which has never been reported before and will be a key point in the understanding of the stability and degradation processes of batteries using LTO as anode.

2. Results and Discussion

Initial film characterization was performed using a multi-technique approach in order to ensure that the desired LTO film was obtained. **Figure S1**a shows the out of plane XRD pattern of the synthesized sample. The most intense peak corresponds to the LTO (111) diffraction line, while higher order diffraction peaks in the same orientation are also present, i.e., (222), (333), (444) and (555). These peaks along with the absence of background are a clear proof that a highly oriented LTO film was obtained. Signal corresponding to the substrate is also visible, as confirmed by the rutile TiO_2 (111) and (222) diffraction lines. Figure S1b shows the surface morphology as measured by SEM. This top view image reveals the existence of cracks that enclose micrometric crystallites which display triangular terraces

aligned in the same direction for all crystallites. These terraces are homogeneously present along the surface and the triangular shape is typical of films and clusters grown on (111)-oriented substrates such as rutile TiO_2 (111) owing to the three-fold symmetry of the substrate. The observed cracks may be the result of a strain release in the LTO film which initially grows following the rutile TiO_2 structure. In Figure S1c, obtained by SEM cross-section analysis, the LTO layer thickness can be estimated around 2.5 μm. Both, cross-section and top-view SEM images also reveal a continuous and pin-hole free LTO layer.

In terms of composition, the LTO film was analysed by means of XPS. From the survey spectra (**Figure S2**a), the presence of the expected elements is confirmed, with no extra contribution from other elements as possible impurities: apart from carbon which is present as adventitious carbon (Figure S2b), typically found in samples exposed to air.[65] Main peak in O 1s region (Figure S2c) is located at a binding energy of 529.3 eV and corresponds to the oxygen in the LTO. There are other less intense contributions to O 1s at higher binding energies (peaks at around 531 eV and over 532 eV), associated to surface species as previously reported[54,55]. The Ti 2p region (Figure S2d) shows the splitting of $2p_{1/2}$ (463.6 eV) and $2p_{3/2}$ (457.9 eV) orbitals, these binding energies are in agreement with the presence of a Ti(IV) oxide[66], as is the case for LTO. Presence of lithium is also confirmed by the detection of Li 1s photoelectron signal (Figure S2e), being part of it related to LTO but also to the surface species already mentioned. The concentrations of the different elements conforming the LTO phase are close to the expected from a stoichiometric point of view, being the atomic ratios O/Ti = 2.5 and O/Li = 3.0. The XRD and XPS data, along with surface and cross-section morphology images of the sample, shown in Figure S1 and Figure S2 confirm that the thin film synthesis process resulted in a pure, homogeneous and highly oriented LTO layer.

Electrochemical response of the LTO layer was verified by cyclic voltammetry (CV) (**Figure 1**). Current peaks related to the reduction and oxidation reactions occurring in LTO material can be observed slightly displaced from 1.55 V (Figure 1a), where these redox reactions

should take place.[12,41] In this case, reduction and oxidation peaks were situated at 1.44 V and 1.66 V respectively, thus, symmetrically displaced 0.11 V from the expected voltage. This hysteresis effect was, most probably, due to the limited electronic conductivity of the system originated by: first, the intrinsic insulating nature of LTO, which in the sample under study was not mixed with any conductive additive, as is usually done for conventional electrodes; and, secondly, from the difficulties arisen from the configuration of the active-material/current-collector connection which, as the LTO layer lies on top of non-conductive TiO_2 substrate, was achieved through a direct contact of the copper current collector at the edges of the LTO film surface. In the CV curve, the oxidation peak is more intense than the reduction one, phenomenon that can be explained by the lower reduction rate compared to the oxidation rate, caused by the different conductivity properties between the starting $Li_4Ti_5O_{12}$ phase and the Li-inserted $Li_7Ti_5O_{12}$,[67] which are electronic insulator and conductive respectively.[68,69] The small peak around 1.30 V during reduction might be related to surface lithium storage process corresponding to the faradaic reaction, as reported before.[70] Rutile TiO_2 single crystal substrates were also tested under the same conditions (Figure 1a), confirming that the substrate is electrochemically inactive and all reported activity can be assigned to LTO.

Figure 1b shows the result of the first four discharge-charge cycles of the LTO electrode. Reversible Li insertion/extraction was obtained with an initial discharge capacity of 54 $\mu A\,h\,cm^{-2}\,\mu m$ (90% of the theoretical value) at a cycling rate of C/20.

In order to verify the formation of the passivating α-Li_2TiO_3 thin layer on top of the LTO (111) upon cycling, both pristine and cycled samples were analysed by surface XRD in a synchrotron source (**Figure 2**). As the eventual formation process of the α-Li_2TiO_3 phase is not fully described, the cycled sample was studied after six full discharge-charge electrochemical processes. The surface diffraction pattern of the pristine sample (Figure 2a) shows the same main features described for Figure S1 which corresponds to LTO (111) single

crystal. However, there are some less intense contributions on the surface diffraction pattern (**Figure 3**), at 2θ = 14.7° and 2θ = 30.0° which are related to the first and second order diffraction of a metastable cubic phase with space group $Fm\bar{3}m$ and lattice parameter a = 4.03 Å, as estimated from the experimental data fitting. These correspond to the (111) and (222) diffraction lines of α-Li_2TiO_3 (111) that has a theoretical lattice parameter a = 4.23 Å. The main peaks observed in Figure 3 correspond to the (222) and (444) diffraction lines of LTO (111) which has a theoretical lattice parameter a = 8.35 Å whilst the experimental lattice parameter determined from the fitting of the experimental data would be a = 8.14 Å. In both cases, there is a cell contraction around 2-4 % along the surface normal direction which would be consistent with a tensile stress within the plane of the LTO layer. As the α-Li_2TiO_3 (111) diffraction peaks are present in the pristine sample (non-cycled), it would imply that α-Li_2TiO_3 is a product of the synthesis process, and not a consequence of the reactions occurring upon the first electrochemical cycles. Similar surface diffraction pattern was obtained for the electrochemically cycled sample (Figure 2b), with no new contribution that may suggest formation of new phases upon cycling. Indeed, a close comparison of the surface diffraction pattern around 2θ = 30.0° before and after six full electrochemical cycles (**Figure 4**) suggests that the α-Li_2TiO_3 phase does not evolve upon electrochemical cycling.

To further study the presence and distribution of the α-Li_2TiO_3 phase in the LTO surface, cross-section analysis was carried out by TEM. Although LTO and α-Li_2TiO_3 present different crystalline structures, spinel and rock-salt respectively, they have several interplanar distances in common that makes difficult to distinguish those phases. However, by checking in the reciprocal space along some particular zone of axis, i.e. [110], it is observed that the LTO presents reflections corresponding to forbidden reflections for the α-Li_2TiO_3 (see **Figure S3**). The absence of certain reflections arises only from the crystal structure and can be used as feature to determine the presence of a given phase in a material. **Figure 5**a shows a TEM image around the surface of the LTO where a difference on the crystal structure can be

discerned around 15 nm from the surface. When performing the Fast Fourier Transform (FFT) in the outermost area of the surface (first 10 nm), it is obtained a diffraction pattern (Figure 5b-left) that can be fully indexed as a rock salt structure corresponding to the α-Li_2TiO_3 phase. On the other hand, by looking at the diffraction in a deeper area into the sample (around 20 nm), all the reflections (Figure 5c-left) can be indexed as a spinel structure corresponding to the LTO phase (Figure 5c-right) which is in agreement with the X ray diffraction data. Thus it is found that the α-Li_2TiO_3 phase is mainly present in the outermost surface region of the LTO.

An additional advantage of achieving high spatial resolution around the surface by means of cross-sectional TEM is that the distribution of the phases can be determined by analysing locally the FFTs, see Figure 6. In the FFT of Figure 6b, some characteristic reflections for LTO (blue squares) and for α-Li_2TiO_3 (red circles) have been highlighted. The reflections for each phase can be separately taken by placing some masks over them and then, by computing the inverse of the FFT of the filtered (or masked) FFT images, it is possible to obtain a filtered image in the real space (this filtering procedure is explained in the workflow diagram of **Figure S4**). In the resulting filtered image, Figure 6c, the red region should correspond to α-Li_2TiO_3 while the blue one should be LTO, however, instead of blue, a violet region is visible and thereby further considerations must be stressed at this point. The reflections marked with red circles in Figure 6b could correspond either to LTO or α-Li_2TiO_3 and no distinction would be possible without other statement. On the other hand, the reflections marked with blue squares can only correspond to the LTO, this because of the forbidden reflections for α-Li_2TiO_3. Thus the violet region will correspond to the intersection between LTO/α-Li_2TiO_3 (red) and LTO (blue) therefore LTO, and the red region should only correspond to the α-Li_2TiO_3. Therefore, from the filtered images in Figure 6, it is confirmed the presence of α-Li_2TiO_3 and it is observed the transition from α-Li_2TiO_3 to LTO in the subsurface region around 10-20 nm underneath the outermost surface.

The lattice strain variation with high spatial resolution at the sample surface was analysed using HREBSD. With this method, elastic strain variations and lattice rotations can be calculated based on the shifts in features of the Kikuchi diffraction pattern (**Figure 7**) collected from the sample surface. In this study, the HREBSD technique is used to measure the relative elastic strain. Please note the resulting frame used to describe the strain state from EBSPs has the x1 direction which corresponds to the sample crystal direction of [011], the x2 direction corresponds to the [101] and the x3 direction corresponds to the [111] surface normal direction as is illustrated in **Figure 8**a.

The out of plane of residual normal strain (ε33) maps obtained using the cross-correlation analysis of the sample before and after electrochemical cycling respectively are shown in Figure 8a. The reference point is a user selected point as indicated by a black circle for each sample on the ε33 strain map. The resulting maps represent the variation of the elastic strain with respect to the marked reference point. The same colour scale (blue to red) is used for each strain map on both samples. Region with high tensile strain are indicated in red, regions with compressive strain are indicated in blue and regions with lower strain or no strain are indicated in green.

Comparing both maps, the variation in the out of plane ε33 strain component maps remains close to zero for the sample before cycling and the variation in the normal strain is higher after cycling. This would be in agreement with the presence of a thin α-Li_2TiO_3 layer as observed by TEM. These type of analysis are also represented by histograms (Figure 8b), where the probability distribution for the ε_{33} normal strain value is plotted. Here the elastic strain variation relative to the mean value across the mapped region of the sample is used. Before cycling, strain variation data follow a Gaussian-like curve centred at zero which corresponds to the mean value which is unknown for the HREBSD measurement but was evaluated as 2-4% compression by the XRD measurement. The width of this Gaussian

distribution is larger than the ~0.02% spread that would be anticipated from the measurement noise [64], but relatively small (~0.06%) compared to the mean strain value (2-4%). After cycling, however, there is a wider distribution of strain values about the mean value, which to repeat is not obtained from the HREBSD measurements but could be implied from XRD data given a stress free lattice parameter. Therefore, a significant increase in the spatial variation of normal strain on the surface for the cycled LTO sample in comparison to the non-cycled one was detected. This increase in the strain variation could be related to the corrugation of the surface during the first lithium insertion-extraction processes that was reported in previous studies.[58]

3. Conclusion

Micron thick highly oriented LTO (111) films have been successfully synthesized and electrochemically cycled versus Li metal and used as model systems to understand the surface evolution of LTO. From the characterisation carried out in pristine and cycled samples, we have proved that no crystalline long range phase is formed on the LTO (111) surface upon electrochemical cycling. In particular, synchrotron-based surface XRD and cross-section TEM results suggest that α-Li_2TiO_3 is a naturally occurring phase in the pristine LTO surface preparation and not formed upon electrochemical cycling as stated in previous studies. Moreover, the increase in the variation of the out of plane residual strain of the cycled surface determined by HRBESD cross-correlation analysis suggests that LTO is not completely free from strain upon cycling. The measured increase in surface strain variation could have been interpreted in previous experimental works by scanning probe microscopy as surface corrugation during the first electrochemical cycles; even the increase in surface corrugation determined by DFT on non-polarized α-Li_2TiO_3/LTO surfaces against vacuum could be seen as a result in line with the surface strain variation increase in the real liquid-solid interface studied in this work. Certainly, the starting system contains α-Li_2TiO_3 and LTO, two species with significantly different lattice constant, therefore polarization in a half cell will induce

modifications in the LTO surface structure upon cycling to accommodate the surface energy changes that result in the observed strain variation increase. Being present on the electrode-electrolyte interface, controlling these surface effects will help to improve even more the already good electrochemical properties of LTO and thus, enhance the battery cyclability in the very long term. Ultimately enhancing their performance in certain applications such as the stationary energy storage, where LTO is already being used as active material on the negative electrode.

4. Experimental Section

Thin Film Synthesis: Due to the requirements of this study, instead of the usual $Li_4Ti_5O_{12}$ synthesis path using TiO_2 and Li_2CO_3 powders as raw materials, rutile TiO_2 (111) single crystal was used as a substrate and LiOH as chemical reagent following a solid state synthesis reported before.[67] Pre-treatment was applied to a commercial 10 x 10 x 0.5 mm rutile TiO_2 (111) single crystal (SurfaceNet) substrate by ultrasonic cleaning both in ethanol and acetone, followed by a calcination process in air at 800 °C for 12 hours. For the $Li_4Ti_5O_{12}$ synthesis process, the single crystal substrate was placed in an alumina crucible along with $LiOH{\cdot}H_2O$ (Sigma-Aldrich, >98%) and heated to 900 °C for 24 hours in air, in order to obtain a $Li_4Ti_5O_{12}$ (111) thin film on its surface.

Thin Film Characterization: Phase and structure of the LTO thin film was checked by out of plane X-ray Diffraction using Bruker Advance D8 instrument with Cu radiation (Cu $K_{\alpha 1,2}$ = 1.5406 Å, 1.5444 Å). Synchrotron Surface X-ray Diffraction was performed at BM25-SpLine in the European Synchrotron (ESRF, Grenoble) with an energy of 20.6 keV (λ = 0.62 Å). In this case, the 2θ scale of the raw spectra was shifted by -0.155 ° to account for small differences in the position of the sample surface with respect to the position of the surface calibration plane. Further structural information was obtained by means of TEM analysis on the cross sections of the samples. Cross sectioning was prepared by the conventional method of embedding the film in epoxy, fixation on Cu grid, thinning by mechanical polishing and

ultimate polishing by the ion milling technique. TEM images and diffraction data were collected by using a FEI Tecnai G2 instrument, with a 200 kV field emission gun (FEG). The surface morphology was characterized by Quanta 200 FEG (FEI) Scanning Electron Microscope (SEM) at 30 kV accelerating voltage. A Zeiss Merlin FEG SEM with 25 keV beam energy with a Bruker eFlash was used to carry out HREBSD measurements. An EBSD pattern size of 800 x 600 selected with exposure time of 1s per pattern and a scanning step size of 220 nm were used. The cross-correlation analysis of the Kikuchi patterns was done by the XEBSD MATLAB code described by Britton & Wilkinson.[71,72]

XPS measurements were conducted at using a Phoibos 150 spectometer coupled to a non-monochromatic Mg K_α source ($h\nu$ = 1253.6 eV). Data were treated with CasaXPS software, and binding energy calibration was set by using the aliphatic carbon signal (284.8 eV).

Electrochemical Measurements: Cyclic Voltametry (CV) and Galvanostatic Cycling (GC) were performed using Biologic VMP3 potentiostats with Swagelok-type cells (polypropylene body) in a two electrode configuration. Cells were assembled in a MBraun Ar filled glove box (H_2O and O_2 values below 0.1 ppm), using metallic lithium (Rockwood Lithium, battery grade) as counter and reference electrode, glass fibre as separator and $LiPF_6$ 1M in ethylene carbonate and dimethyl carbonate (EC:DMC, 1:1 in volume) as electrolyte (Solvionic, 99.9%). Copper was used as current collector in the thin film side. CV measurements were performed at 0.05 mV s^{-1} rate, while C/20 current rate was used in the case of GC.

Supporting Information

Supporting Information is available from the Wiley Online Library or from the author.

Acknowledgements

We would like to acknowledge the support of the European Commission under the Project "Stable Interfaces for Rechargeable Batteries" (SIRBATT) (FP7-ENERGY-2013, grant agreement No. 608502). A.V.-C. and A. J. W. acknowledge activity on a grant funded by the Engineering and Physical Research Council in UK as contributing to this work: nanoscale characterisation of nitride films (EP/ J016098/1)

References

[1] J.-M. Tarascon, M. Armand, *Nature* **2001**, *414*, 359.
[2] K. Ozawa, Ed. , *Lithium Ion Rechargeable Batteries: Materials, Technology, and New Applications*, Wiley, **2009**.
[3] O. K. Park, Y. Cho, S. Lee, H.-C. Yoo, H.-K. Song, J. Cho, *Energy Environ. Sci.* **2011**, *4*, 1621.
[4] F. T. Wagner, B. Lakshmanan, M. F. Mathias, *J. Phys. Chem. Lett.* **2010**, *1*, 2204.
[5] B. Dunn, H. Kamath, J.-M. Tarascon, *Science* **2011**, *334*, 928.
[6] Z. Yang, J. Zhang, M. C. W. Kintner-Meyer, X. Lu, D. Choi, J. P. Lemmon, J. Liu, *Chem. Rev.* **2011**, *111*, 3577.
[7] M. S. Whittingham, *Chem. Rev.* **2014**, *114*, 11414.
[8] N. Nitta, F. Wu, J. T. Lee, G. Yushin, *Mater. Today* **2015**, *18*, 252.
[9] A. Deschanvres, B. Raveau, Z. Sekkal, *Mater. Res. Bull.* **1971**, *6*, 699.
[10] D. C. Johnston, *J. Low Temp. Phys.* **1976**, *25*, 145.
[11] K. M. Colbow, J. R. Dahn, R. R. Haering, *J. Power Sources* **1989**, *26*, 397.
[12] S. Scharner, W. Weppner, P. Schmid-Beurmann, *J. Electrochem. Soc.* **1999**, *146*, 857.
[13] T. Ohzuku, A. Ueda, N. Yamamoto, *J. Electrochem. Soc.* **1995**, *142*, 1431.
[14] S. Panero, P. Reale, F. Ronci, B. Scrosati, P. Perfetti, V. R. Albertini, *Phys. Chem. Chem. Phys.* **2001**, *3*, 845.
[15] F. Ronci, P. Reale, B. Scrosati, S. Panero, V. Rossi Albertini, P. Perfetti, M. di Michiel, J. M. Merino, *J. Phys. Chem. B* **2002**, *106*, 3082.
[16] M. Wagemaker, D. R. Simon, E. M. Kelder, J. Schoonman, C. Ringpfeil, U. Haake, D. Lützenkirchen-Hecht, R. Frahm, F. M. Mulder, *Adv. Mater.* **2006**, *18*, 3169.
[17] H. M. Wu, I. Belharouak, H. Deng, A. Abouimrane, Y.-K. Sun, K. Amine, *J. Electrochem. Soc.* **2009**, *156*, A1047.
[18] J. Haetge, P. Hartmann, K. Brezesinski, J. Janek, T. Brezesinski, *Chem. Mater.* **2011**, *23*, 4384.
[19] K. Zaghib, M. Dontigny, A. Guerfi, P. Charest, I. Rodrigues, A. Mauger, C. M. Julien, *J. Power Sources* **2011**, *196*, 3949.
[20] D. Peramunage, K. M. Abraham, *J. Electrochem. Soc.* **1998**, *145*, 2609.
[21] Z. Yang, D. Choi, S. Kerisit, K. M. Rosso, D. Wang, J. Zhang, G. Graff, J. Liu, *J. Power Sources* **2009**, *192*, 588.
[22] J. B. Goodenough, *Energy Storage Mater.* **2015**, *1*, 158.
[23] J. Christensen, V. Srinivasan, J. Newman, *J. Electrochem. Soc.* **2006**, *153*, A560.
[24] A. Singhal, G. Skandan, G. Amatucci, F. Badway, N. Ye, A. Manthiram, H. Ye, J. J. Xu, *J. Power Sources* **2004**, *129*, 38.
[25] K. Amine, I. Belharouak, Z. Chen, T. Tran, H. Yumoto, N. Ota, S.-T. Myung, Y.-K. Sun, *Adv. Mater.* **2010**, *22*, 3052.
[26] H.-G. Jung, M. W. Jang, J. Hassoun, Y.-K. Sun, B. Scrosati, *Nat. Commun.* **2011**, *2*, 516.
[27] J. B. Goodenough, K.-S. Park, *J. Am. Chem. Soc.* **2013**, *135*, 1167.
[28] Y.-J. Hao, Q.-Y. Lai, J.-Z. Lu, H.-L. Wang, Y.-D. Chen, X.-Y. Ji, *J. Power Sources* **2006**, *158*, 1358.
[29] M. Ganesan, M. V. T. Dhananjeyan, K. B. Sarangapani, N. G. Renganathan, *J. Electroceramics* **2007**, *18*, 329.
[30] J. Kim, J. Cho, *Electrochem. Solid-State Lett.* **2007**, *10*, A81.
[31] C. Jiang, E. Hosono, M. Ichihara, I. Honma, H. Zhou, *J. Electrochem. Soc.* **2008**, *155*, A553.

[32] E. Matsui, Y. Abe, M. Senna, A. Guerfi, K. Zaghib, *J. Am. Ceram. Soc.* **2008**, *91*, 1522.
[33] A. S. Prakash, P. Manikandan, K. Ramesha, M. Sathiya, J.-M. Tarascon, A. K. Shukla, *Chem. Mater.* **2010**, *22*, 2857.
[34] J. Huang, Z. Jiang, *Electrochem. Solid-State Lett.* **2008**, *11*, A116.
[35] S.-L. Chou, J.-Z. Wang, H.-K. Liu, S.-X. Dou, *J. Phys. Chem. C* **2011**, *115*, 16220.
[36] L. Shen, E. Uchaker, X. Zhang, G. Cao, *Adv. Mater.* **2012**, *24*, 6502.
[37] L. Yu, H. B. Wu, X. W. (David) Lou, *Adv. Mater.* **2013**, *25*, 2296.
[38] S. Zhao, O. Ka, X. Xian, L. Sun, J. Wang, *Electrochimica Acta* **2016**, *206*, 17.
[39] Z. Ding, L. Zhao, L. Suo, Y. Jiao, S. Meng, Y.-S. Hu, Z. Wang, L. Chen, *Phys. Chem. Chem. Phys.* **2011**, *13*, 15127.
[40] L. Zhao, Y.-S. Hu, H. Li, Z. Wang, L. Chen, *Adv. Mater.* **2011**, *23*, 1385.
[41] L. Shen, X. Zhang, E. Uchaker, C. Yuan, G. Cao, *Adv. Energy Mater.* **2012**, *2*, 691.
[42] Y.-Q. Wang, L. Gu, Y.-G. Guo, H. Li, X.-Q. He, S. Tsukimoto, Y. Ikuhara, L.-J. Wan, *J. Am. Chem. Soc.* **2012**, *134*, 7874.
[43] C. H. Chen, J. T. Vaughey, A. N. Jansen, D. W. Dees, A. J. Kahaian, T. Goacher, M. M. Thackeray, *J. Electrochem. Soc.* **2001**, *148*, A102.
[44] K.-S. Park, A. Benayad, D.-J. Kang, S.-G. Doo, *J. Am. Chem. Soc.* **2008**, *130*, 14930.
[45] H. Zhao, Y. Li, Z. Zhu, J. Lin, Z. Tian, R. Wang, *Electrochimica Acta* **2008**, *53*, 7079.
[46] J. Shu, *Electrochem. Solid-State Lett.* **2008**, *11*, A238.
[47] L. E. Ouatani, R. Dedryvère, C. Siret, P. Biensan, D. Gonbeau, *J. Electrochem. Soc.* **2009**, *156*, A468.
[48] R. Dedryvère, D. Foix, S. Franger, S. Patoux, L. Daniel, D. Gonbeau, *J. Phys. Chem. C* **2010**, *114*, 10999.
[49] Y.-B. He, B. Li, M. Liu, C. Zhang, W. Lv, C. Yang, J. Li, H. Du, B. Zhang, Q.-H. Yang, J.-K. Kim, F. Kang, *Sci. Rep.* **2012**, *2*, 913.
[50] Y.-B. He, F. Ning, B. Li, Q.-S. Song, W. Lv, H. Du, D. Zhai, F. Su, Q.-H. Yang, F. Kang, *J. Power Sources* **2012**, *202*, 253.
[51] I. Belharouak, G. M. Koenig, T. Tan, H. Yumoto, N. Ota, K. Amine, *J. Electrochem. Soc.* **2012**, *159*, A1165.
[52] V. Borgel, G. Gershinsky, T. Hu, M. G. Theivanayagam, D. Aurbach, *J. Electrochem. Soc.* **2013**, *160*, A650.
[53] Y.-B. He, M. Liu, Z.-D. Huang, B. Zhang, Y. Yu, B. Li, F. Kang, J.-K. Kim, *J. Power Sources* **2013**, *239*, 269.
[54] T. Nordh, R. Younesi, D. Brandell, K. Edström, *J. Power Sources* **2015**, *294*, 173.
[55] J.-B. Gieu, C. Courrèges, L. El Ouatani, C. Tessier, H. Martinez, *J. Power Sources* **2016**, *318*, 291.
[56] X. Lu, L. Zhao, X. He, R. Xiao, L. Gu, Y.-S. Hu, H. Li, Z. Wang, X. Duan, L. Chen, J. Maier, Y. Ikuhara, *Adv. Mater.* **2012**, *24*, 3233.
[57] F. Wang, L. Wu, C. Ma, D. Su, Y. Zhu, J. Graetz, *Nanotechnology* **2013**, *24*, 424006.
[58] M. Kitta, T. Akita, Y. Maeda, M. Kohyama, *Langmuir* **2012**, *28*, 12384.
[59] B. J. Morgan, J. Carrasco, G. Teobaldi, *J. Mater. Chem. A* **2016**, *4*, 17180.
[60] T. B. Britton, J. Jiang, Y. Guo, A. Vilalta-Clemente, D. Wallis, L. N. Hansen, A. Winkelmann, A. J. Wilkinson, *Mater. Charact.* **2016**, *117*, 113.
[61] A. J. Wilkinson, *Ultramicroscopy* **1996**, *62*, 237.
[62] A. J. Wilkinson, P. B. Hirsch, *Micron* **1997**, *28*, 279.
[63] A. J. Wilkinson, G. Meaden, D. J. Dingley, *Mater. Sci. Technol.* **2006**, *22*, 1271.
[64] A. J. Wilkinson, G. Meaden, D. J. Dingley, *Ultramicroscopy* **2006**, *106*, 307.
[65] T. L. Barr, S. Seal, *J. Vac. Sci. Technol. A* **1995**, *13*, 1239.
[66] M. C. Biesinger, L. W. M. Lau, A. R. Gerson, R. St. C. Smart, *Appl. Surf. Sci.* **2010**, *257*, 887.

[67] M. Kitta, T. Akita, Y. Maeda, M. Kohyama, *Appl. Surf. Sci.* **2012**, *258*, 3147.
[68] C. Kim, N. S. Norberg, C. T. Alexander, R. Kostecki, J. Cabana, *Adv. Funct. Mater.* **2013**, *23*, 1214.
[69] M. G. Verde, L. Baggetto, N. Balke, G. M. Veith, J. K. Seo, Z. Wang, Y. S. Meng, *ACS Nano* **2016**, *10*, 4312.
[70] C. Lai, Y. Y. Dou, X. Li, X. P. Gao, *J. Power Sources* **2010**, *195*, 3676.
[71] T. B. Britton, A. J. Wilkinson, *Ultramicroscopy* **2011**, *111*, 1395.
[72] T. B. Britton, A. J. Wilkinson, *Ultramicroscopy* **2012**, *114*, 82.

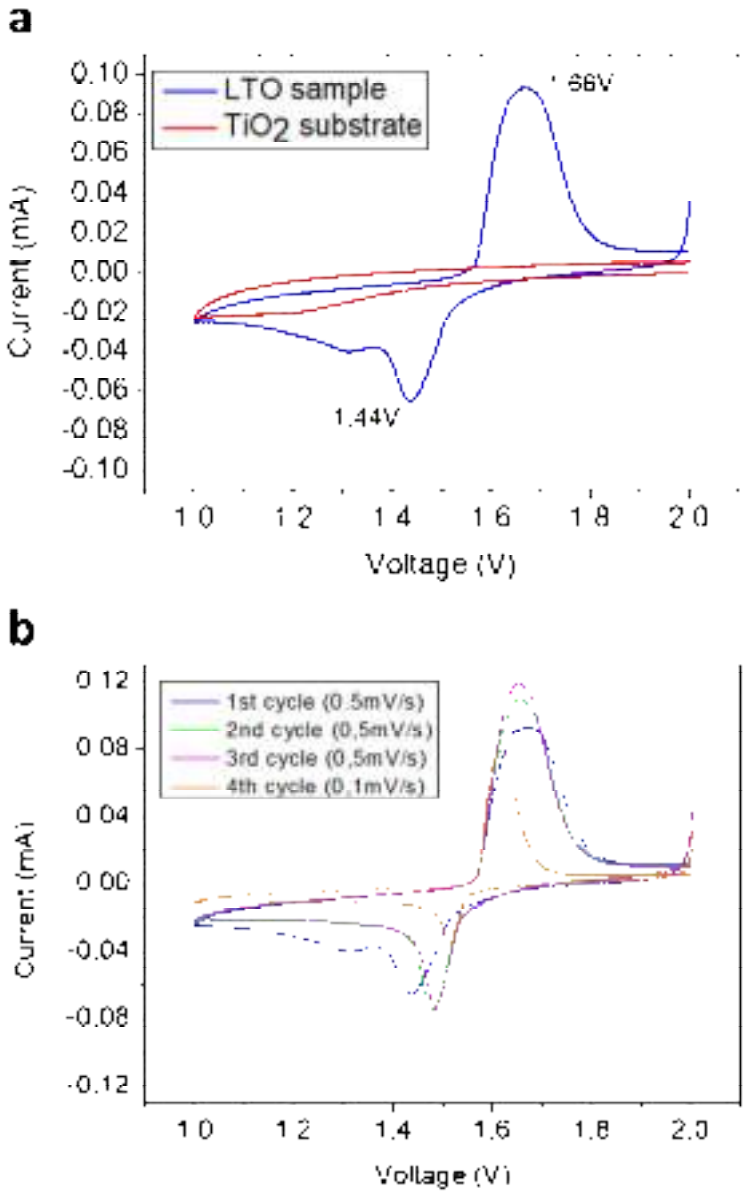

Figure 1. Electrochemical tests performed on the electrodes: (a) cyclic voltammetry for the synthesized LTO sample and for the rutile TiO_2 substrate; and (b) cyclic voltammetry of the LTO during the first 4 cycles.

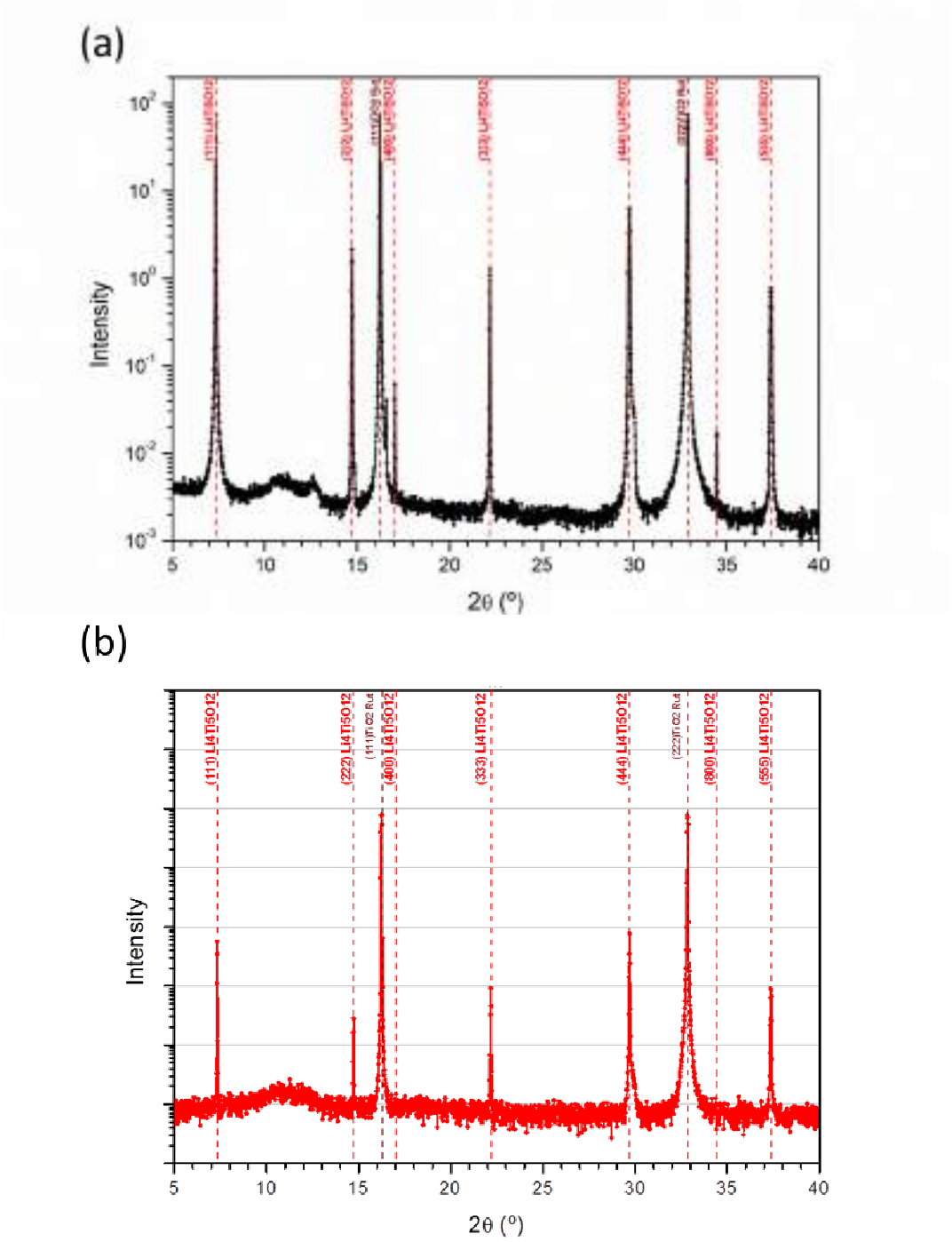

Figure 2. Surface XRD pattern using a synchrotron radiation source (hν = 20.6 keV) from the (a) pristine LTO and (b) cycled LTO electrodes. In both patterns, the theoretical position of the $Li_4Ti_5O_{12}$ (111), (222), (333), (444), (555), (400), (800) and TiO_2 (111) and (222) is included for reference.

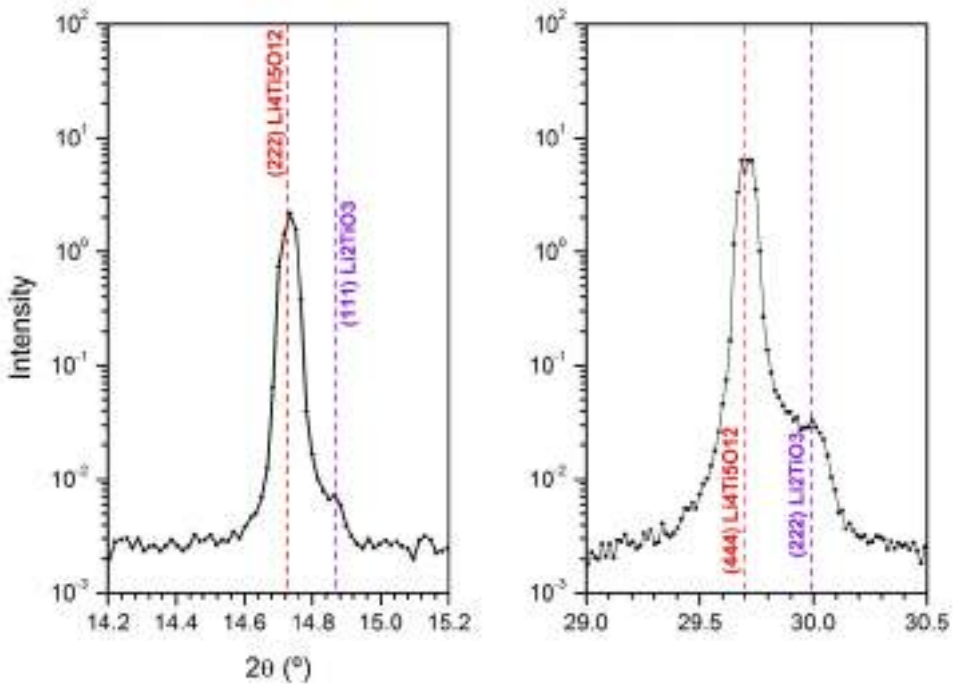

Figure 3. Detail of the synchrotron radiation surface (hν = 20.6 keV) diffraction pattern at 2θ = 14.7° and 2θ = 30.0° from the pristine sample. Positions of $Li_4Ti_5O_{12}$ (222) and (444) diffraction peaks and α-Li_2TiO_3 (111) and (222) are highlighted in red and purple respectively.

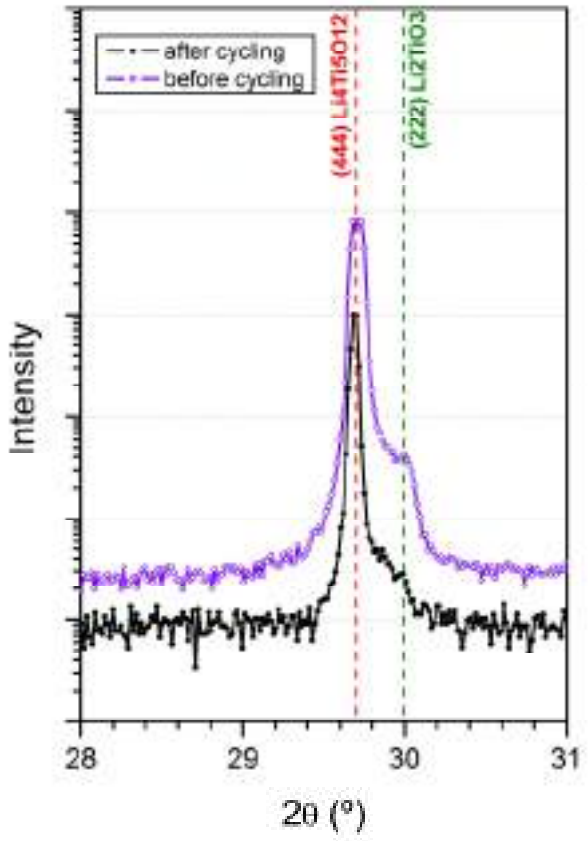

Figure 4. Surface diffraction peaks measured with synchrotron radiation (hν = 20.6 keV) corresponding to LTO (444) and α-Li_2TiO_3 (222) planes before (black) and after (purple) electrochemical cycling.

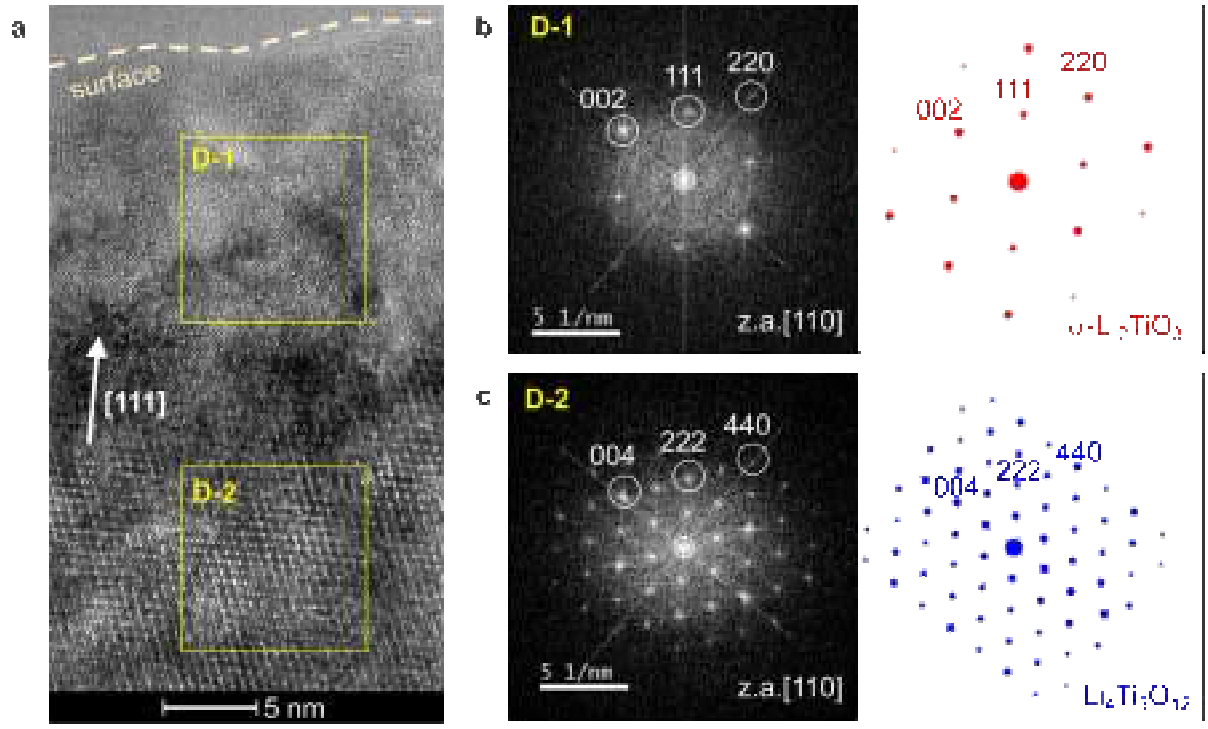

Figure 5. (a) Cross-section TEM result from the LTO sample surface. (b) On the left, local FFT obtained from region D-1 and, on the right, electron diffraction pattern computed for α-Li_2TiO_3 with z.a. [111]. (c) On the left, local FFT obtained from region D-2 and, on the right, electron diffraction pattern computed for $Li_4Ti_5O_{12}$ with z.a. [111].

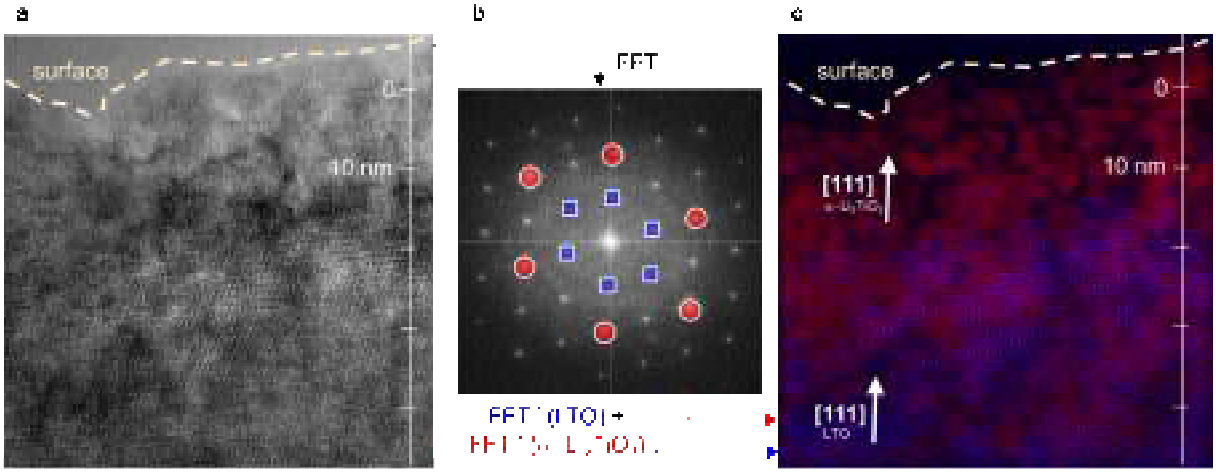

Figure 6. TEM image around the LTO surface (a) and its global FFT (b). (c) Filtered FFT^{-1} obtained by adding two FFT^{-1}: the first computed by selecting only the reflections corresponding to the LTO (blue-squares) and the second by selecting only the reflections corresponding to α-Li_2TiO_3 (red-circles). The Filtered FFT^{-1} allows to observe the spatial distribution of phases. Color code: α-Li_2TiO_3 area in red and LTO in violet (ideally LTO should be blue but reflections from LTO and α-Li_2TiO_3 are very close).

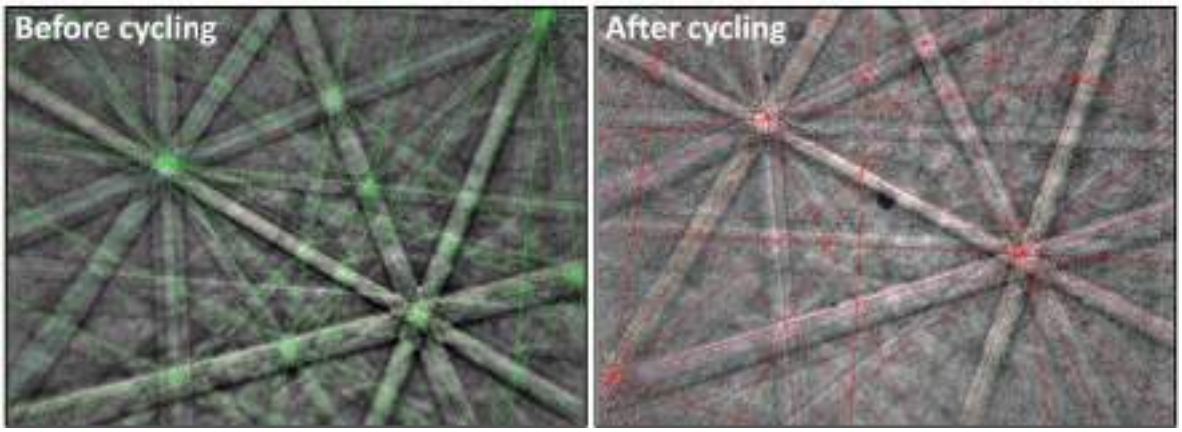

Figure 7. Experimental Kikuchi patterns obtained by HREBSD along with their corresponding fit for the pristine (left, green) and electrochemically cycled (right, red) samples.

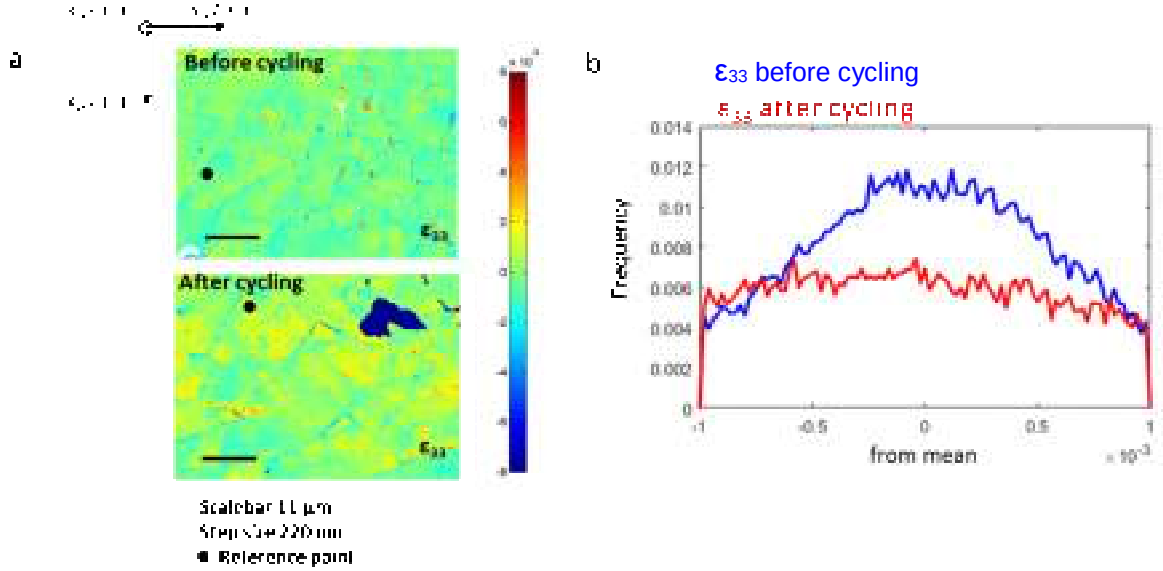

Figure 8. Residual ε_{33} strain mapped by EBSD for the LTO electrode before and after cycling (a), and the distribution of ε_{33} normal strain (b)

High resolution electron backscattering diffraction and high resolution transmission electron microscopy are used to proof that the zero-strain and SEI-free lithium titanate (LTO) used as anode in commercial Li-ion batteries undergoes a significant increase of the surface strain upon electrochemical cycling. The understanding of the LTO surface evolution upon electrochemical cycling will help to improve the stability and cycling performance of next generation Li-ion batteries.

Keyword
$Li_4Ti_5O_7$, surface reactivity, HREBSD, XPS, HRTEM

J. Rikarte, B. Acebedo, A. Vilalta-Clemente, F. Bonilla, A. J. Wilkinson, M. Galceran, A. Lousa, J. Rubio-Zuazo, M. A. Muñoz-Márquez*

Surface Evolution of Lithium Titanate upon Electrochemical Cycling using a Combination of Surface Specific Characterization Techniques

ToC figure ((Please choose one size: 55 mm broad × 50 mm high **or** 110 mm broad × 20 mm high. Please do not use any other dimensions))

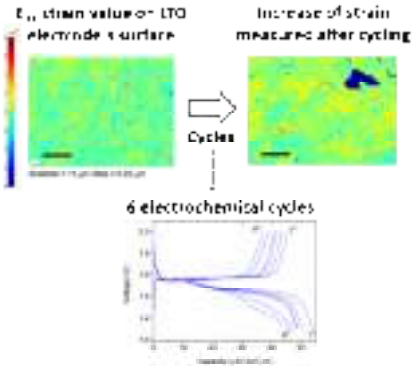

Supporting Information

Surface Evolution of Lithium Titanate upon Electrochemical Cycling using a Combination of Surface Specific Characterization Techniques

*Jokin Rikarte, Begoña Acebedo, Arantxa Vilalta-Clemente, Francisco Bonilla, Angus J. Wilkinson, Montserrat Galceran, Arturo Lousa, Juan Rubio-Zuazo, Miguel A. Muñoz-Márquez**

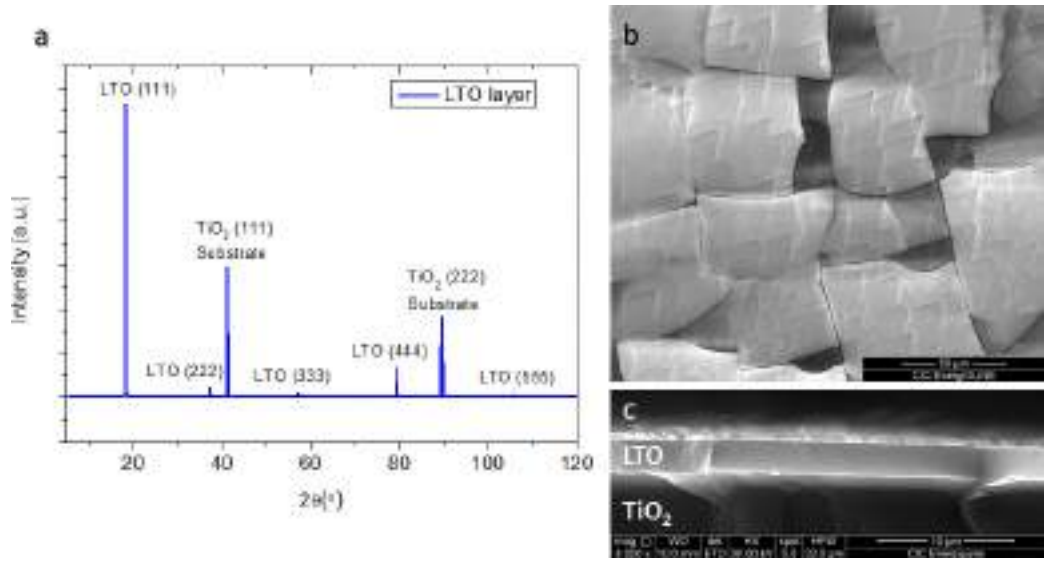

Figure S1. X-Ray Diffraction pattern of the synthesized LTO sample (a), and surface morphology (b) and cross-section analysis (c) studied both by SEM.

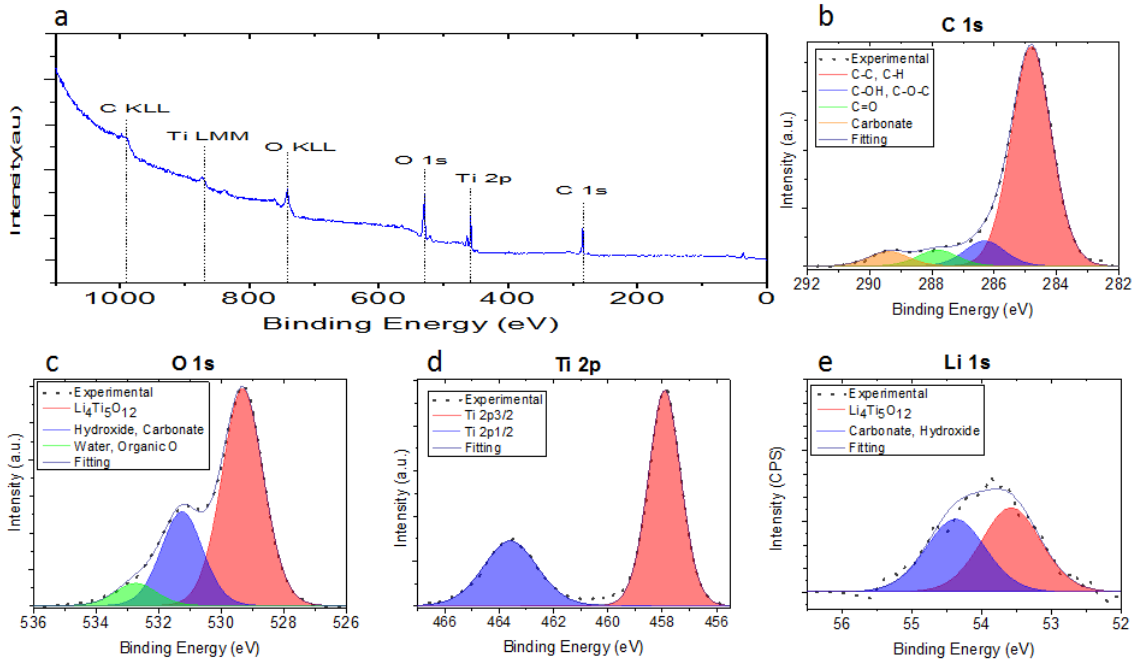

Figure S2. XPS results. Survey spectra (a), and the specific regions analyzed for C1s (b), O 1s (c), Ti 2p (d) and Li 1s (e).

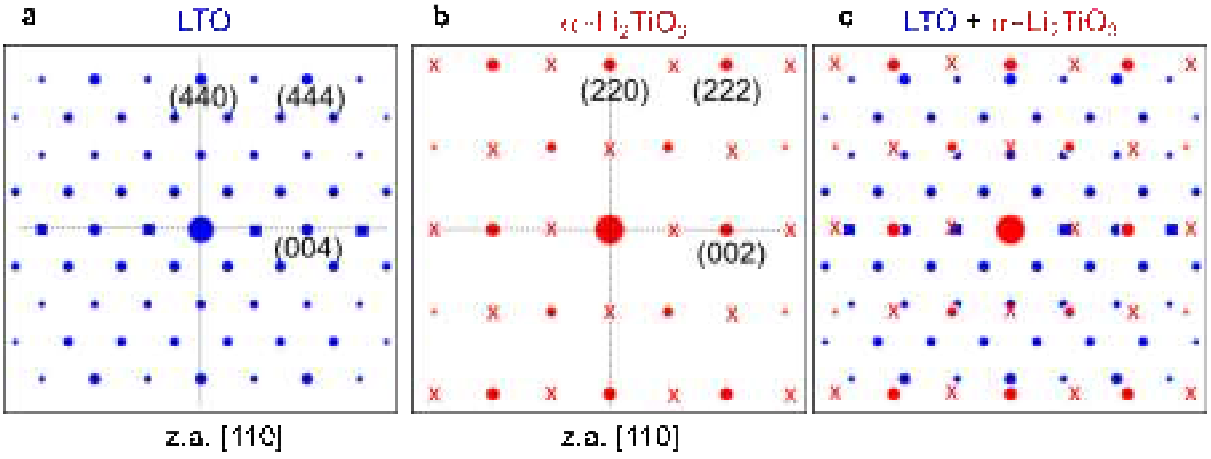

Figure S3. Diffraction patterns computed with zone of axis [110] for LTO (a) and α-Li_2TiO_3 (b). (c) sum of patterns (a) and (b); in agreement with X ray diffraction, the reflections of α-Li_2TiO_3 are almost overlap all the LTO reflections. Forbidden diffraction reflections for the α-Li_2TiO_3 phase are indicated with crosses (x).

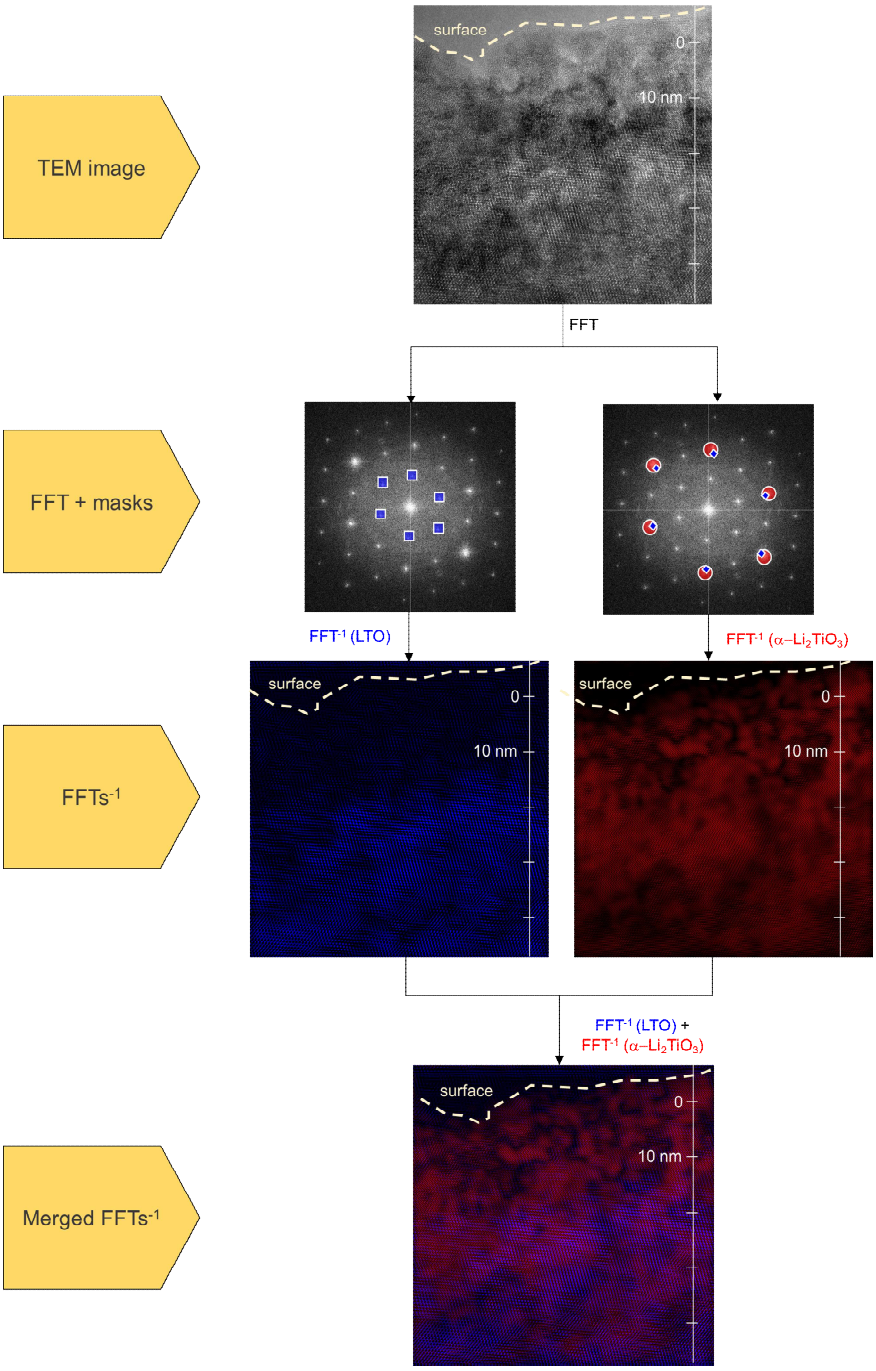

Figure S4. Workflow diagram for obtaining a filtered FFT^{-1} image from a TEM image. Initially a FFT image is computed from the whole TEM image. Then, masks are placed over the reflections corresponding to each phase (the masks allow to isolate the information contained into them from the outside or other reflections). Then the inverse FFT (or FFT^{-1}) is computed from each masked FFT image. This produces a filtered image per phase, where the color intensity represents the distribution of the phase, with black being no presence of the phase. Finally, the different FFTs-1 images are merged on a single image which combines the colors of each phase and thereby showing the spatial distribution of the phases. Here violet and red represent LTO and α-Li_2TiO_3 respectively.